Journal of Applied Fluid Mechanics, Vol. 17, No. 9, pp. 1993-2004, 2024.
Available online at www.jafmonline.net, ISSN 1735-3572, EISSN 1735-3645.
https://doi.org/10.47176/jafm.17.9.2553

Numerical Study on the Influence of Plasma Actuation on the Cavitation Characteristics of Hydrofoil

R. Guo[1,2†], L. Wang[1] , R. Li[1,2] and X. Zhang[1]

[1] *School of Energy and Power Engineering, Lanzhou University of Technology, Lanzhou,730050, China*
[2] *Key Laboratory of Fluid Machinery and Systems, Gansu Province, Lanzhou,730050 China*

†Corresponding Author Email: guorong@lut.edu.cn

ABSTRACT

In order to investigate the influence of plasma actuation on cavitation in the flow field around a hydrofoil, the RNG *k-ε* turbulence model with density correction, the Schnerr–Sauer cavitation model, and the plasma phenomenological model were used to analyze the influence of forward and reverse plasma actuation on the cavitation characteristics of the NACA66(MOD) hydrofoil at an angle of attack of 8. The cavitation number of the incoming flow was 0.99. The results showed that under the positive excitation condition, the cavitation volume on the suction side of the hydrofoil was reduced by about 30%, and the time-averaged lift–drag ratio was reduced by about 5%, which had little influence on the re-entrant jet, vortex and shear flow. Therefore, the cavitation suppression effect on the hydrofoil flow field was weak. Under the condition of reverse actuation, the volume of cavitation on the suction side of the hydrofoil was reduced by about 87%, and the time-averaged lift–drag ratio was increased by about 21%, which effectively worsened the development conditions of cavitation. By greatly reducing the intensity of the re-entrant jet and eliminating the vortex and shear flow in the flow field, cavitation in the hydrofoil flow field was obviously suppressed. This shows that reasonable plasma actuation is an effective means to control hydrofoil cavitation.

Article History

Received December 31, 2023
Revised February 22, 2024
Accepted March 27, 2024
Available online July 2, 2024

Keywords:

Cavitation
Hydrofoil
Plasma actuation
Re-entrant jet
Vortex structure

1. INTRODUCTION

Hydrofoils are the smallest components of fluid machinery and are often used in pumps (Thomai & Chatterjee, 2015), ships (Kumagai et al., 2015), and submarines (Deng et al., 2021). Hydrofoil cavitation refers to the phenomenon where water vapor on the hydrofoil surface is rapidly generated in the low-pressure area and suddenly collapses in the high-pressure area under the impact of water flow. Cavitation leads to the appearance of bubbles on the surface of the hydrofoil, deteriorating the performance of the machine (Wang & Brennen, 1999; Look et al., 2019;). Therefore, it is very important to improve the cavitation flow field and suppress and weaken the damage caused by hydrofoil cavitation to improve efficiency and maintain safe and stable operation (Liu et al., 2019; Pant & Frankel, 2021).

Scholars have conducted a large amount of research work on hydrofoil cavitation (Li et al., 2021; Podnar et al., 2021;Gu et al., 2022; Yang et al., 2023). Zhao et al. (2023) realized the overall and local control of a cavitation flow field by optimizing the profile and adding a continuous flow control structure, which effectively improved the cavitation and hydrodynamic performance of a hydrofoil. Kawanami et al. (1997) studied the mechanism of hydrofoil cloud cavitation by setting obstacles with a certain height on the suction side of the hydrofoil and revealed the relationship between the re-entrant jet and cloud cavitation. The above research has made an important contribution to people's understanding of the evolution mechanism of hydrofoil cavitation, but the influence of the active control method on hydrofoil cavitation characteristics needs further study.

Plasma, primarily composed of free electrons and charged ions, is often referred to as the fourth state of matter and exhibits unique electromagnetic properties. Plasma actuation is a technique that leverages the properties of plasma for the active control of fluid flow. Its fundamental principle involves the use of electromagnetic forces to induce directed movement of plasma clusters or changes in physical properties such as pressure and velocity due to gas discharge, thereby applying a controllable disturbance to the local flow field. Numerous researchers have done related work on the

NOMENCLATURE

a	height of the plasma equivalent action region triangle *OAB*	p	mixed phase pressure
b	length of the plasma equivalent action region triangle *OAB*	R_B	cavity radius
c	hydrofoil chord	u	mixed phase velocity
c_μ	model constant	U	actuation voltage
d	electrode spacing	v	vapor phases
e	electron charge constant	α	volume fraction
E_0	electric field strength at the origin	ρ_m	mixed phase density
E_b	maximum electric field strength	ρ_c	charge density,
F_{vap}	evaporation coefficient	μ_m	mixed phase laminar viscosity coefficient
F_{cond}	condensation coefficient	μ_t	mixed phase turbulence viscosity coefficient
i , j	coordinate direction	ε	dissipation rate of turbulent kinetic energy
l	liquid phase	γ_1	voltage actuation frequency
$\dot{m}^+$	fluid evaporation rate	δ	dirac delta function
$\dot{m}^-$	fluid condensation rate	Δt	plasma action time in one actuation cycle
n	density correction index	UDF	User-Defined Functions
n_b	number of cavities		

interaction between plasma and flow field (Li et al., 2022). Wang et al. (2016) numerically simulated the flow around the column under the DBD plasma effect, and found that the method could reduce the drag coefficient and change the vortex shedding frequency. Yu and Zheng (2023) used nanosecond pulsed plasma actuation to control the aerodynamic performance of hydrofoil separated flow, and revealed that the effect of flow control depends on the plasma actuation frequency, and the best control effect can be obtained when the frequency is close to the natural frequency of the shear layer in the reference flow. Guo et al. (2022) conducted a numerical study on plasma control of axial tip clearance leakage flow in liquid ring pumps. The study found that plasma actuation can effectively suppress the leakage flow intensity and reduce flow losses. An important condition for cavitation is that the local pressure is lower than the saturated vapor pressure of the liquid. Plasma actuation changes the flow velocity and direction by applying a controllable disturbance to the local flow field, thus affecting the pressure distribution of the flow field, thus destroying the conditions for cavitation and hindering the development of cavitation nuclei.

The Dielectric Barrier Discharge (DBD) plasma actuation (Zhang & Wang, 2023) generates an electric field by applying a high voltage between two electrodes, ionizing gas molecules to create plasma, which in turn stimulates the flow of the fluid field. In this study, the DBD plasma actuation method, coupled with the phenomenological model, the RNG k-ε turbulence model with density correction, and the influence of the plasma actuation on the hydrofoil cavitation characteristics, was studied numerically.

2. NUMERICAL METHOD

2.1 Physical Model

The 2D NACA66(MOD) hydrofoil is used for numerical simulation and analysis. The chord length of the hydrofoil is 70 mm, the maximum thickness at a distance from the leading edge of the hydrofoil is x = 0.45c, the maximum camber is 2%, and the distance from the leading edge is x = 0.50c. The flow area is a rectangle, as presented in Fig.1.

2.2 Grid Division and Boundary Conditions

The hydrofoil calculation domain was divided into hexahedral structured grids, which were completed using ICEM CFD 19.0. To accurately capture the flow field in detail, the near-wall area of the hydrofoil was encrypted with the grid height of the first layer located in the viscous bottom layer, as presented in Fig. 2.

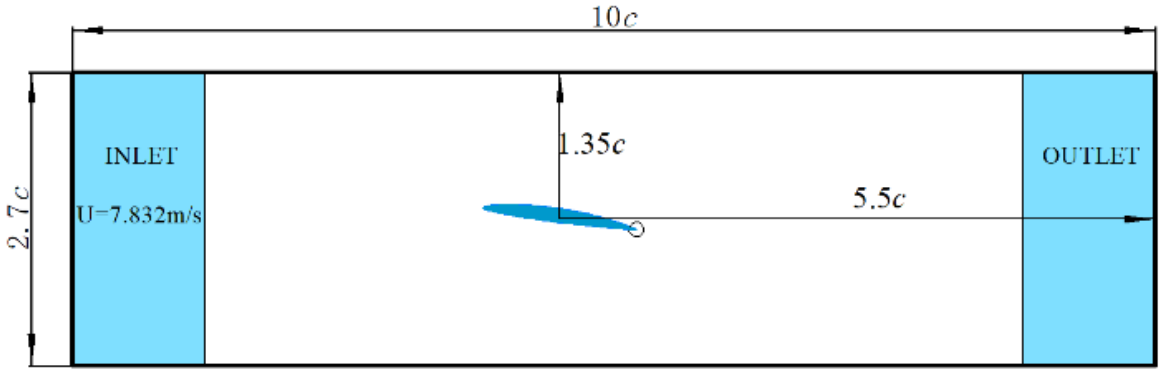

Fig. 1 Numerical simulation domain and hydrofoil's position

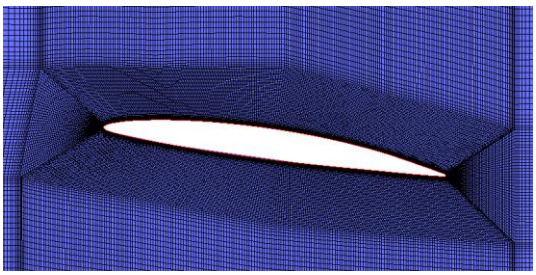

(a) Hydrofoil grid

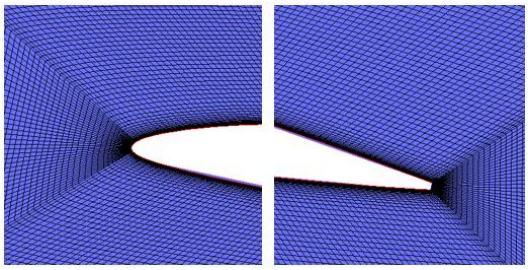

(b) Local grid

Fig. 2 Grid schematic

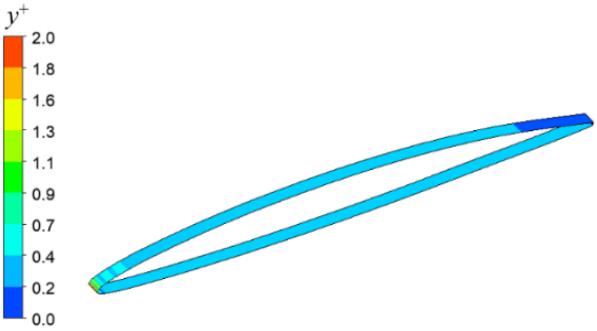

Fig. 3 Grid wall y^+ distribution

To satisfy the requirements of enhanced wall function on the wall boundary layer mesh, the y^+ near the hydrofoil was checked, as presented in Fig.3. It could be seen that $y^+ < 2$ met the calculation requirements.

To negate the impact of mesh count and quality on the accuracy of computational simulations, five distinct sets of grids with varied quantities were created for grid independence analysis, as presented in Table 1.

It is evident from Mesh3 that the lift and drag coefficients calculated after continued encryption have become stable. In order to save computing resources, Mesh3 grids are used in the numerical simulation of the two-dimensional hydrofoil, and the total number of grids is 113708.

Table 1 Comparative analysis of lift and drag coefficient of five grids.

Mesh	Nodes	$C_l \times 10^2$	$C_d \times 10^3$
Mesh1	70380	52.284	87.035
Mesh2	92720	52.411	87.065
Mesh3	113708	52.559	87.053
Mesh4	132293	52.675	87.054
Mesh5	152000	52.676	87.055

The numerical simulation of the hydrofoil cavitation flow field was carried out using ANSYS Fluent 19.0, and the unsteady cavitation flow field was calculated with the calculation result of the steady cavitation flow field as the initial value. Using the boundary conditions of velocity inlet and pressure outlet, the hydrofoil surface and the upper and lower wall boundaries were all no-slip walls. The inlet velocity was 7.832 m/s, the angle of attack was 8, and the cavitation number was 0.99. Based on the pressure solver and SIMPLEC algorithm, the turbulence model was the RNG k-ε model with density correction, and the cavitation model was the Schnerr–Sauer cavitation model. The pressure term was in PRESTO! and each convective term was in Second-Order Upwind. The transient solution format was Second-Order Implicit, and the time step of the unsteady calculation was $\Delta t=5.0\times10^{-4}$.

2.3 Governing Equation

Drawing from the homogeneous equilibrium flow model's foundational equations (Saurel & Lemetayer, 2001), the continuity and momentum equations pertinent to the vapor–liquid biphasic system are delineated below:

$$\frac{\partial \rho_m}{\partial t}+\frac{\partial(\rho_m u_j)}{\partial x_j}=0 \tag{1}$$

$$\frac{\partial \rho_m \mu_i}{\partial t}+\frac{\partial(\rho_m \mu_i \mu_j)}{\partial x_j}=-\frac{\partial p}{\partial x_i}+\frac{\partial}{\partial x_j}[(\mu_m+\mu_t)(\frac{\partial \mu_i}{\partial x_j}+\frac{\partial \mu_j}{\partial x_i}-\frac{2}{3}\frac{\mu}{\partial x_j}\delta_{ij})] \tag{2}$$

The density and viscosity of the mixed phase are

$$\rho_m=\rho_l\alpha_l+\rho_v\alpha_v \tag{3}$$

$$\mu_m=\mu_l\alpha_l+\mu_v\alpha_v \tag{4}$$

2.4 Turbulence Model

Because the original turbulence model was established for single-phase flow, the phase transition and compressibility characteristics were not fully considered, and the turbulent viscosity of the hole tail was over-predicted during the simulation of cavitation flow, resulting in a larger viscous force than the actual one in the hole tail region, and preventing the backflow structure in the flow field from moving upstream due to insufficient energy. Therefore, a density-modified RNG k-ε turbulence model was adopted in this study. The model adopts a vapor–liquid two-phase mixing density function to refine the adjustment of turbulent viscosity present in the conventional RNG k-ε model (Coutier-Delgosha et al., 2003). In the standard RNG k-ε model, the turbulent viscosity is as follows:

$$\mu_t=\rho c_\mu\frac{k^2}{\varepsilon} \tag{5}$$

The modified turbulence model adopts the following two formulas to calculate turbulence viscosity

$$\mu_t = f(\rho_m) c_\mu \frac{k^2}{\varepsilon} \tag{6}$$

$$f(\rho_m) = \rho_v + \left(\frac{\rho_m - \rho_v}{\rho_l - \rho_v} \right)^n (\rho_l - \rho_v) \tag{7}$$

where c_μ = 0.085, n=3 in this study.

2.5 Cavitation Model

The cavitation model characterized the bidirectional mass transfer between the liquid and vapor phases. Both cavitation formation and collapse should be considered in the model. The study employed the Schnerr–Sauer model (Schnerr & Sauer, 2001) to solve for vapor–liquid phase density. In most of these models, heat transfer and non-equilibrium phase transition effects are ignored, and the transport equation of vapor phase volume fraction is described using the component transfer method:

$$\frac{\partial(\rho_v \alpha_v)}{\partial t} + \nabla(\rho_v \alpha_v u) = \dot{m}^+ - \dot{m}^- \tag{8}$$

$$\alpha_v = \frac{n_b \frac{4}{3} \pi R_B^3}{1 + n_b \frac{4}{3} \pi R_B^3} \tag{9}$$

Thus, the vapor–liquid mass transfer rate of the model is formed as follows:

$$\begin{cases} \dot{m}^+ = F_{vap} \dfrac{\rho_v \rho_l}{\rho_m} \alpha_v (1 - \alpha_v) \dfrac{3}{R_B} \sqrt{\dfrac{2}{3} \dfrac{p_v - p}{\rho_l}} \\ p \le p_v \\ \dot{m}^- = F_{cond} \dfrac{\rho_v \rho_l}{\rho_m} \alpha_v (1 - \alpha_v) \dfrac{3}{R_B} \sqrt{\dfrac{2}{3} \dfrac{p - p_v}{\rho_l}} \\ p > p_v \end{cases} \tag{10}$$

where F_{vap} =50 and F_{cond} =0.2.

2.6 Phenomenological Model of Plasma

There are two arrangements of DBD plasma actuations: symmetric and asymmetric. In this study, the plasma actuation model with an asymmetric structure proposed by Shyy et al (2002) is adopted, which ignores the chemical reaction and specific discharge process caused by discharge and only pays attention to the electric field force generated by the plasma acting on the flow field in the form of momentum. The active area of plasma is equivalent to a right triangle *OAB*, as presented in Fig.4.

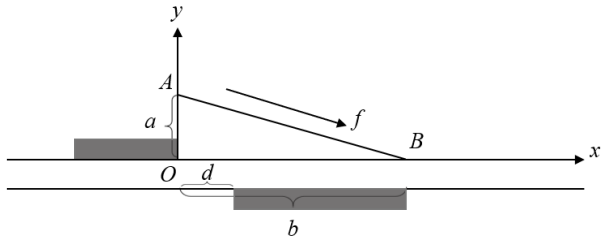

Fig. 4 Action region of plasma actuation

There is a maximum electric field intensity at the origin *O*. The distribution of the electric field force in this region is linear, and the direction points downward along *AB*, which can be expressed as follows:

$$E(x, y) = E_0 - k_1 x - k_2 y \tag{11}$$

$$E_0 = \frac{U}{d} \tag{12}$$

$$k_1 = \frac{E_0 - E_b}{b} \tag{13}$$

$$k_2 = \frac{E_0 - E_b}{a} \tag{14}$$

The component of the electric field strength in the x and y directions can be expressed as follows:

$$E_x = \frac{E(x, y) k_2}{\sqrt{k_1^2 + k_2^2}} \tag{15}$$

$$E_y = \frac{E(x, y) k_1}{\sqrt{k_1^2 + k_2^2}} \tag{16}$$

The body force in the x and y directions can be expressed as follows:

$$f_x = \rho_c e E_x \gamma_1 \Delta t \delta \tag{17}$$

$$f_y = \rho_c e E_y \gamma_1 \Delta t \delta \tag{18}$$

The parameters of the plasma actuation are as follows: a = 2.0 mm, b = 4 mm, and d = 0.25 mm in the equivalent region of action, $\rho_c = 10^{11}$ cm^3, e = 1.6022 × 10^{-19} C, γ_1 = 20 kHz, Δt = 67 μs; U = 15 kV, and E_b = 30 kV/cm. The Dicla function δ is used to determine the boundary of the electric field force; when $E \ge E_0$, we take δ = 1, and for the opposite, it is 0.

$$\delta = \begin{cases} 1, E \ge E_b \\ 0, \text{other} \end{cases} \tag{19}$$

The control of the hydrofoil cavitation flow field by the plasma body force was achieved by writing UDF in Fluent to describe the relationship between the body force and the coordinates and adding the body force source term to the N-S equation.

2.7 Plasma Actuation Control Methods

Plasma actuation was arranged at the highest point of the hydrofoil suction surface (0.19 times the hydrofoil chord length from the leading edge of the hydrofoil). According to the jet direction, it was categorized in the leading edge to trailing edge direction (hereinafter called the forward direction) and the trailing edge to leading edge direction (hereinafter called the reverse direction), as presented in Fig.5. The forward direction was the same as the incoming flow direction and caused downwind jetting; the reverse direction was the opposite of the incoming flow direction and caused upwind jetting.

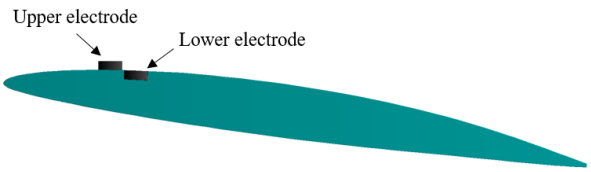

(a) Forward actuation

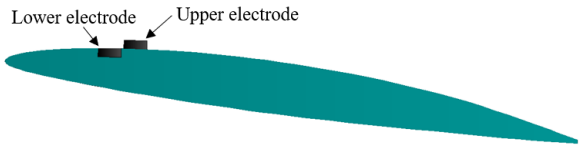

(b) Reverse actuation

Fig. 5 Schematic diagram of the location of the plasma actuation

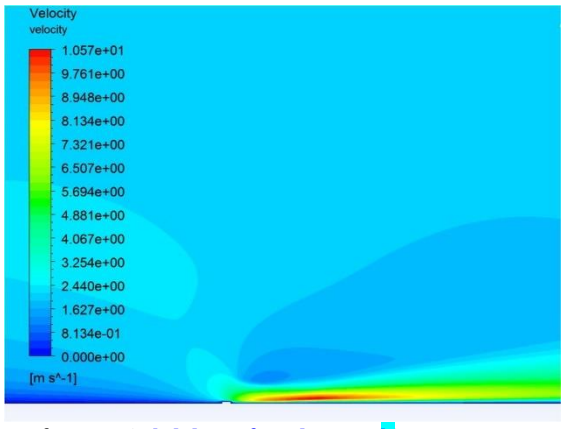

(a) Reference (Abdelraouf et al., 2020b)

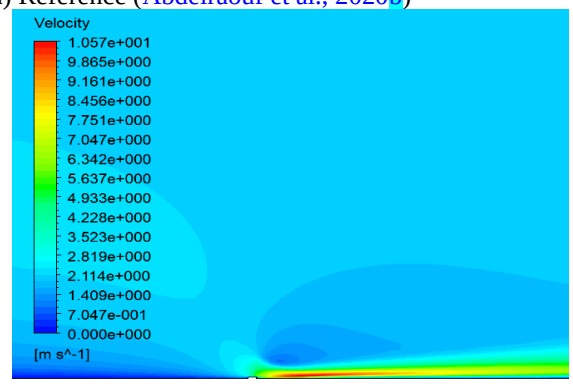

(b) Simulation results of this study

Fig. 6 Velocity contour at velocity inlet 2 m/s

3. MODEL VERIFICATION

3.1 Shyy Model Verification

The calculation domain and actuation position proposed by Abdelraouf et al. (2020) were used to verify the Shyy model, and the actuation parameters were the same as that of Shyy, and the results of the Shyy model are compared with the results of the current calculation simulation. Figure 6 presents the velocity contour at velocity inlet 2 m/s, which is basically consistent with Abdelraouf's work.

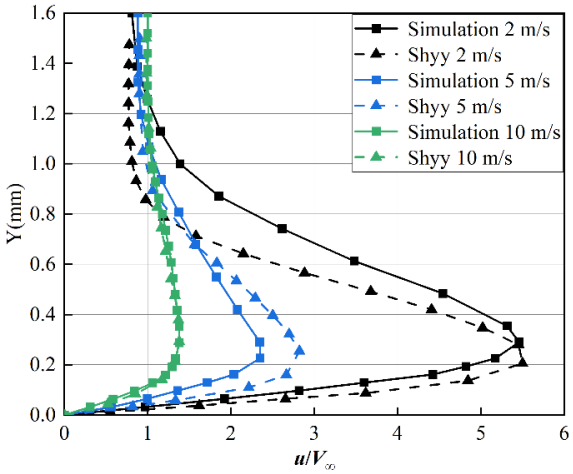

Fig. 7 Velocity distribution at position 3.8 mm after the upper electrode with different inlet velocity magnitude

Figure 7 presents the distribution of different velocities at 3.8 mm behind the upper electrode, which, upon comparison with the findings of Shyy, displays slight differences. However, the overall trend is consistent. This can be attributed to Shyy's study not detailing the numerical settings in the publication. From this observation, it can be ensured that model accuracy is maintained.

3.2 Numerical Model Verification

In order to verify the feasibility of the adopted numerical method, the numerical results were compared with the experimental results. The experimental equipment and conditions were as those used in Ref. (Wang et al., 2020); Fig.8 presents the process of NACA66(MOD) hydrofoil cloud cavitation evolution, and the numerical calculation results clearly described the quasi-periodic changes in cavitation generation, development, and shedding; however, the capture of cloud cavitation shedding on the suction side was somewhat shortened, or the thickness was thinned compared to the experiments. Still, the periodicity and the trend of the changes were basically the same, which indicated that the numerical method was accurate and could be used for further research.

4. RESULTS AND ANALYSIS

4.1 Effect of Plasma Actuation on the Cavitation Morphology of the Hydrofoil

Fig.9 illustrates the variation in the cavitation flow field of the hydrofoil with time in one cycle with three actuation forms, and the pressure contour map (unit Pa) is also presented in the figure. The figure illustrates that under the non-actuation condition, cavitation first appeared in the leading-edge area of the hydrofoil and developed into sheet cavitation attached to the surface; then, the end of sheet cavitation was lifted and gradually transformed into cloud cavitation. When the cavitation

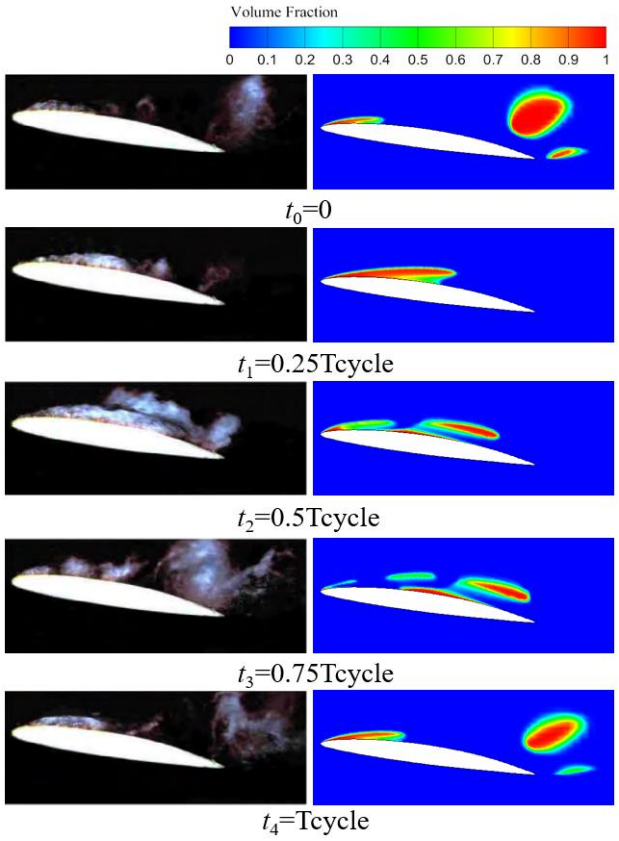

(a) Experimental results (b) Numerical calculations

Fig. 8 Cavitation shape evolution of the NACA66(MOD) hydrofoil

volume reached the maximum downstream of the trailing edge, it fell off and collapsed, and local high pressure formed an adverse pressure gradient at the moment of collapse. Under the condition of forward actuation, the maximum length of the sheet cavitation decreased at 1/4T, and the adverse pressure gradient also decreased. During the period from 1/4T to 3/4T, the cavitation attached to the suction side of the hydrofoil developed slowly after a retraction, and it was not until 3/4T that cloud cavitation appeared on the trailing edge, indicating that the forward actuation prolonged the duration of the sheet cavitation but reduced the existence time of cloud cavitation. Under the condition of reverse actuation, the cavitation above the suction side of the hydrofoil shrank to "quasi-steady" sheet cavitation attached to the leading edge of the hydrofoil, and the cavitation length did not increase after it reached 0.19*c*, and it did not continue to develop into cloud cavitation. The results of the above analysis show that both actuation directions can effectively improve the pressure gradient on the suction side of the hydrofoil and then inhibit cavitation, and the reverse actuation effect is more significant.

Figure 10 (the left ordinate shows the cavitation volume of non-actuation and forward actuation hydrofoils, and the right ordinate shows the cavitation volume of reverse actuation hydrofoils) presents the change process in the cavitation volume in four periods. From the figure, it can be seen that the pulsation period of cavitation volume under the condition of forward actuation was consistent with that under the condition of non-actuation, but the emergence time of the maximum cavitation

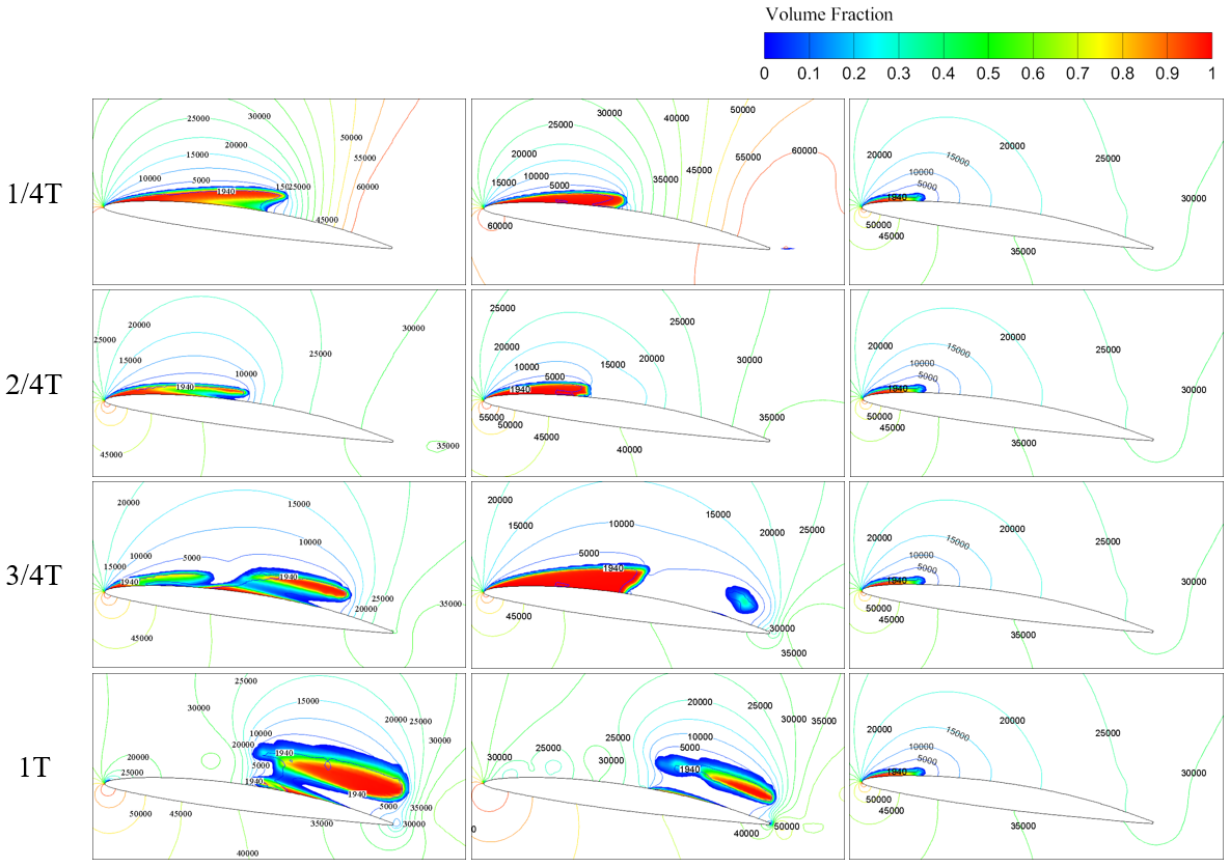

(a) Non-actuation (b) Forward actuation (c) Reverse actuation

Fig. 9 Cavitation shape evolution of the hydrofoil in one cycle

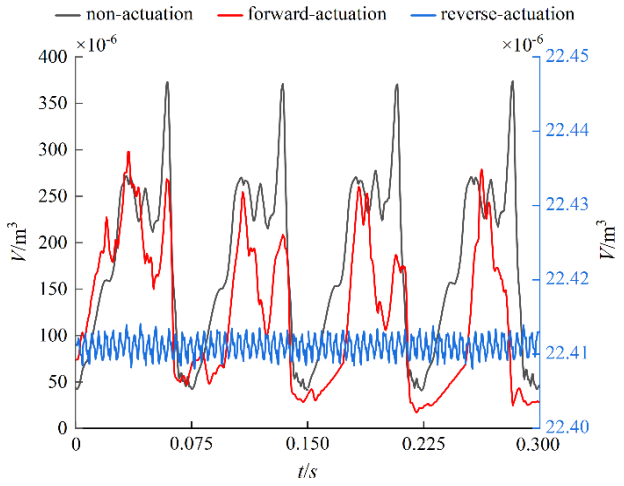

Fig. 10 Cavitation volume before and after actuation

Table 2 Hydrofoil's hydrodynamic properties under different plasma actuation

	C_l	C_d	C_l/C_d
Non-actuation	0.416	0.057	7.298
Forward actuation	0.403	0.058	6.948
Reverse actuation	0.362	0.041	8.829

volume changed, while the pulsation period of the cavitation volume under the condition of reverse actuation was obviously shortened, and the pulsation amplitude was obviously reduced. According to the calculation, the time-averaged cavitation volume of the hydrofoil under the three actuation conditions was about 177cm^3, 123cm^3, and 22cm^3, respectively, which indicated that plasma actuation could effectively suppress cavitation volume, and reverse actuation had the best suppression effect, accounting for only about 13% of the non-actuation condition.

4.2 Effect of Plasma Actuation on the Hydrofoil Hydrodynamic Characteristics

Figure 11 presents the time–domain graphs of the hydrofoil lift–drag coefficient in three actuation forms, and Table 2 contains the influence of the plasma actuation on the hydrofoil lift–drag coefficient. According to the graphs, we can see that forward actuation had little influence on the lift–drag coefficient, but the lift–drag coefficient was obviously reduced, and the change period was shortened when reverse actuation was used, which indicates that reverse actuation makes the hydrofoil cavitation change process more stable.

Combined with Table 2, it can be observed that compared with the non-actuation hydrofoil, the time-averaged lift-to-drag ratio of the forward-actuated hydrofoil decreased by approximately 5%, whereas that of the reverse-actuated hydrofoil increased by around 21%. This suggests that forward actuation has a marginal impact on the hydrofoil's hydrodynamic properties, while reverse actuation significantly enhances them.

In order to more accurately analyze the difference in the hydrodynamic performance of the hydrofoil under the three actuation forms, the lift coefficient was analyzed in the frequency spectrum, as presented in Fig. 12 (the left

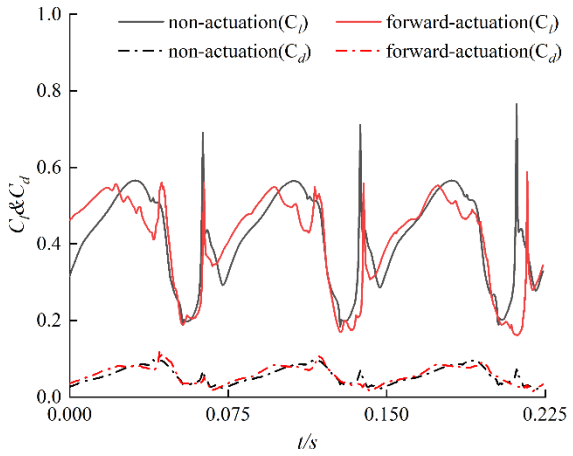

(a) The lift–drag coefficients of non-actuation and forward-actuation hydrofoil

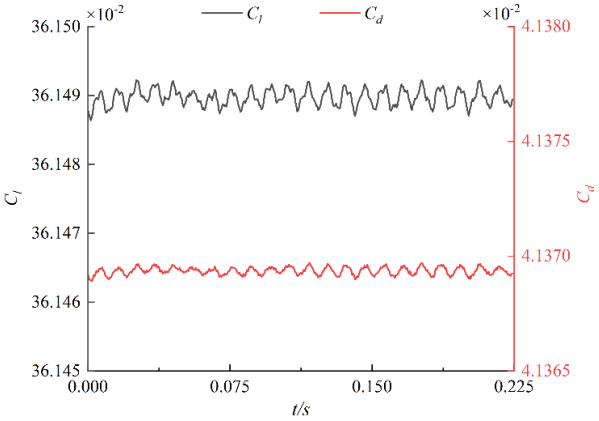

(b) The lift–drag coefficients of the reverse actuation hydrofoil

Fig. 11 Hydrofoil lift–drag coefficient under different plasma actuation

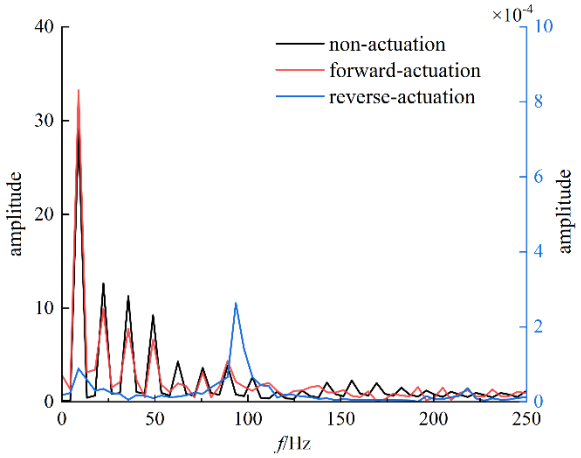

Fig. 12 Hydrofoil lift coefficient spectrum under different plasma actuation conditions

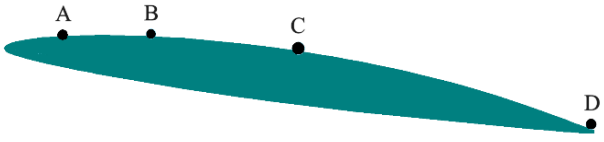

Fig. 13 Monitoring point distribution

ordinate shows the pulsation amplitude of the non-actuation hydrofoil and forward actuation hydrofoil, and the right ordinate shows the pulsation amplitude of the reverse actuation hydrofoil).

It can be seen from the figure that the characteristic frequency of the lift coefficient of the hydrofoil was the same under the conditions of non-actuation and forward actuation, which shows that forward actuation had little influence on the spectral characteristics of the lift coefficient. The first frequency in the spectrum analysis was the dominant frequency of cloud cavitation (Wang et al., 2019), which shows that the vibration amplitude caused by cloud cavitation increased by 13%. Compared with the non-actuation condition, reverse actuation changed the frequency spectrum characteristics of the hydrofoil lift coefficient but also significantly reduced its pulsation amplitude, which was due to the disappearance of the cloud cavitation on the hydrofoil surface before it was suppressed by plasma to 0.19*c* (the highest point), which improved its hydrodynamic characteristics.

4.3 Effect of Plasma Actuation on the Pressure Pulsation Characteristics of the Hydrofoil

The pressure time–frequency characteristics of four characteristic positions (A~D are x=0.1c, x=0.25c, x=0.5c, and x=1.0c, respectively) of the hydrofoil suction surface were quantitatively analyzed, as presented in Fig.13.

Figure 14(a) contains a time–domain diagram of the pressure pulsation at each characteristic position. As can be seen from the diagram, the pressure peak at point A increased by about 10% under the condition of forward actuation, while the pressure peak at points B~D decreased to some extent. During the whole period, the duration of low pressure (P≤5000Pa) at points A, B, and D had no obvious change, and the duration of low pressure at point C was shortened by about 1/4T, which was consistent with the evolution process of the cavitation presented in Fig. 9(b), indicating that forward actuation inhibited the development of cloud cavitation in the second half (0.5c~1c) of the suction side. Under the condition of reverse actuation, the pressure at A was at a low level in the whole cycle. Combined with Fig. 9(c), it can be seen that this point was always surrounded by cavitation, and the peak pressure and low pressure duration at other characteristic positions were obviously improved, indicating that reverse actuation could improve the pressure on the suction side as a whole and inhibit the development of cavitation.

Figure 14(b) (the left ordinate shows the pulsation amplitude of the non-actuation and forward actuation hydrofoils, and the right ordinate shows the pulsation amplitude of the reverse actuation hydrofoils) contains the frequency spectrum of the pressure pulsation at each characteristic position. Under forward actuation, the main frequency of the pressure pulsation at A, B, and D were the same as that without actuation, while the main frequency of the pressure pulsation at C was 6.6 Hz and 33.2 Hz without actuation. As far as the amplitude corresponding to the main frequency was concerned, points A and B were smaller than the non-actuation hydrofoil, and points C and D were larger than the non-actuation hydrofoil, which demonstrates that the pressure pulsation intensity in the suction side of the hydrofoil was weakened by forward actuation, and the pressure pulsation intensity in the range of 0.25c~1c was enhanced. Under the condition of reverse actuation, the main frequency of each characteristic position was between 200 and 300 Hz, and the corresponding amplitude was very small (at least 10^5 orders of magnitude lower than that of the non-actuation hydrofoil), which shows that reverse actuation had a significant impact on the pressure pulsation spectrum characteristics of the suction side, and it obviously improved.

4.4 Effect of the Plasma Actuation on the Re-entrant Jet Characteristics of the Hydrofoil

The re-entrant jet forms as fluid flows in the reverse direction along the suction side of the hydrofoil due to the presence of an adverse pressure gradient, severing sheet cavitation and triggering the development of cloud cavitation (Wang et al., 2017). The dimensionless number C_{re} is used to define the strength of the re-entrant jet:

$$C_{re}=\frac{p-p_v}{p_v}\frac{\rho vL}{\mu}=\left(\frac{p}{p_v}-1\right)Re_1 \tag{20}$$

where p is the average pressure near the start of the re-entrant jet, p_v is the saturated vapor pressure, ρ is the fluid density, v is the re-entrant jet velocity, L is the characteristic size of the contact surface between the re-entrant jet and the cavitation, and μ is the dynamic viscosity.

The size of C_{re} is closely related to cavitation morphology. When C_{re} reaches 10^4, the cavitation morphology in the flow field is sheet cavitation. When C_{re} reaches the order of 10^5, the cavitation form in the flow field is cloud cavitation, and when C_{re} reaches the order of 10^6, the cavitation form interacts strongly with the re-entrant jet and changes dramatically.

The distribution of the hydrofoil streamline and re-entrant jet in three actuation forms is described in Fig. 15. As illustrated in the figure, compared with the non-actuation hydrofoil, the intensity of the re-entrant jet on the suction side of the hydrofoil was reduced by different degrees at the characteristic moment, and the intensity of the re-entrant jet on the suction side of the hydrofoil was obviously weakened and thinned by reverse actuation. Through quantitative analysis of the strength of the re-entrant jet, it was established that the re-entrant jet strength on the suction side of the hydrofoil was about 2.89×10^6, 2.03×10^6, and 6.71×10^4 under the conditions of non-actuation, forward actuation, and reverse actuation, respectively. The above results show that although the re-entrant jet strength could be weakened to some extent by forward actuation, the cavitation and the re-entrant jet were still on a strong interaction level. The inhibition effect on the development of cavitation was limited, while reverse actuation could obviously reduce the re-entrant jet strength and its interaction with cavitation; thus, the cavitation in the hydrofoil flow field could be obviously suppressed.

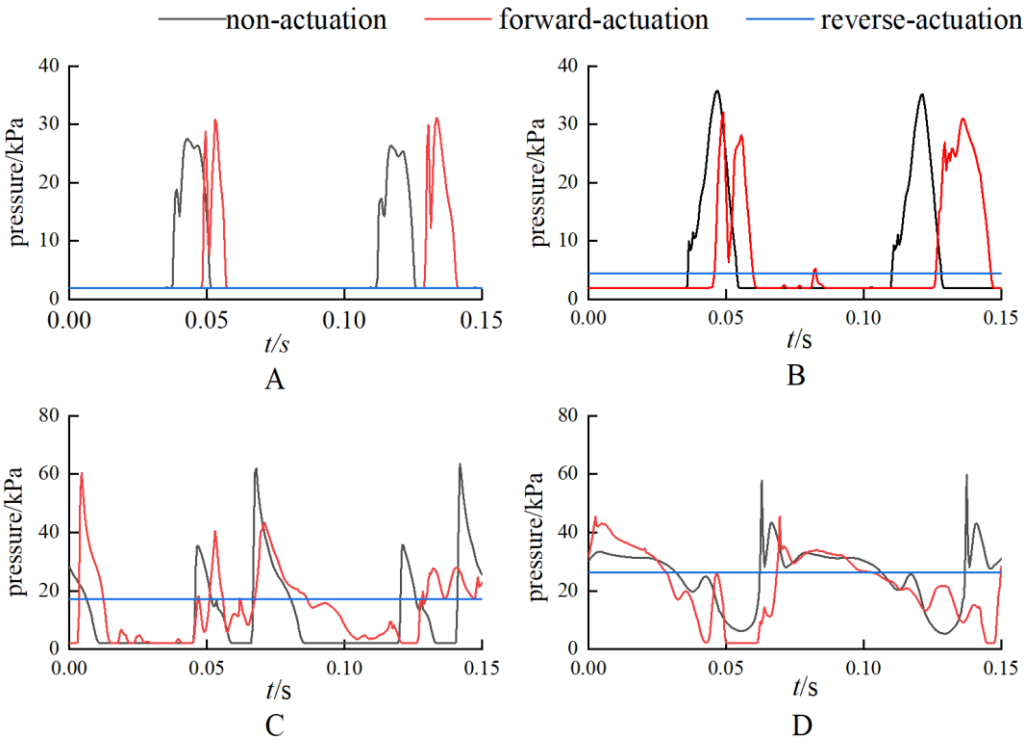

(a) Waveform of plasma actuation pulsation on hydrofoil pressure

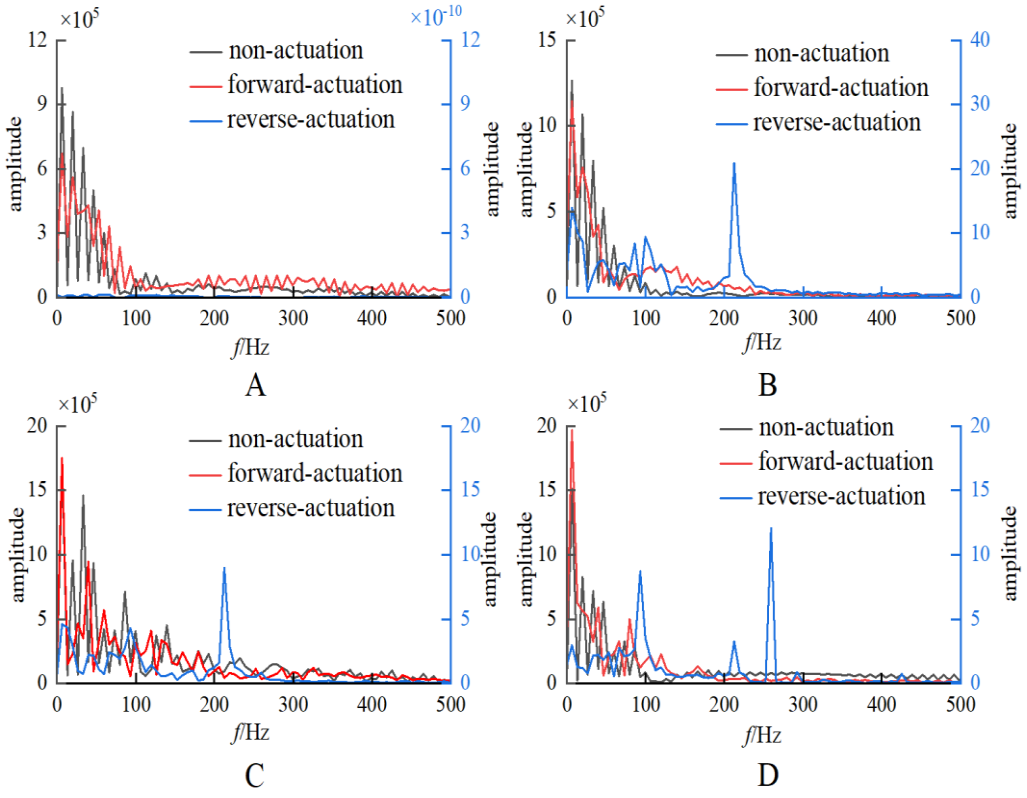

(b) Spectrogram of plasma actuation pulsation on hydrofoil pressure

Fig. 14 Waveform and spectrogram of plasma actuation pulsation on hydrofoil pressure

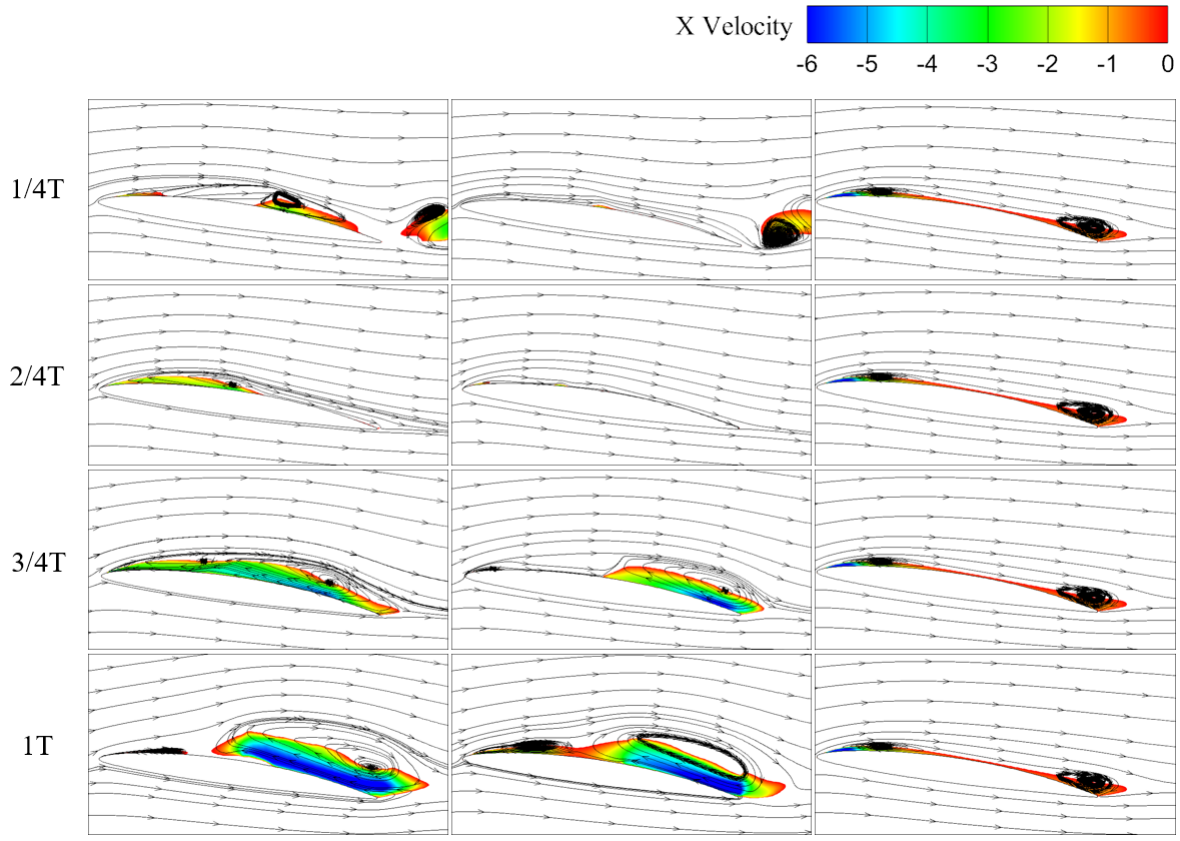

(a) Non-actuation (b) Forward-actuation (c) Reverse-actuation

Fig. 15 Distribution of hydrofoil streamlines and re-entrant jets before and after plasma actuation

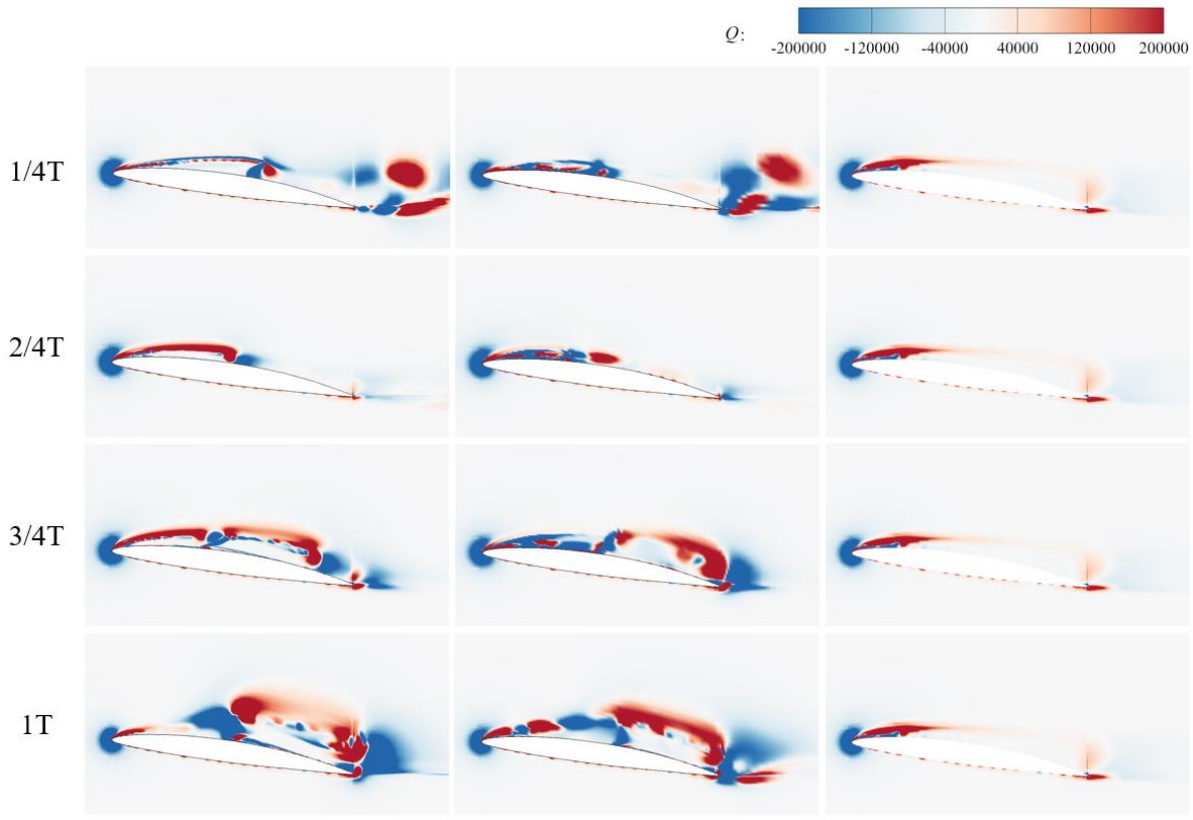

(a) Non-actuation (b) Forward actuation (c) Reverse actuation

Fig. 16 Q distribution cloud of different hydrofoils before and after plasma actuation

4.5 Effect of the Plasma Actuation on the Vortex and Shear Characteristics of the Hydrofoil

Q is the second invariant of the velocity gradient tensor under Galilean transformation, which can clearly reflect the vortex structure and shear motion in the flow field. $Q>0$ is the vortex, the local maximum positive value can be used to identify the vortex core, and $Q<0$ is the shear flow area. The larger the Q, the stronger the vortex motion, and the smaller the Q, the greater the shear force. In a two-dimensional flow field, Q is defined as follows:

$$Q = \frac{\partial U}{\partial x}\frac{\partial V}{\partial y} - \frac{\partial V}{\partial x}\frac{\partial U}{\partial y}. \tag{21}$$

The Q distribution of the hydrofoil under three actuation modes is presented in Fig. 16. The information in the figure demonstrates that the positive value of Q was consistent with the outer contour area of cavitation, and the negative value correlated with the exterior outline area of the re-entrant jet, which indicates that there was obvious vortex motion and shear motion around the leading-edge sheet cavitation and trailing-edge cloud cavitation with the high vapor content of the hydrofoil. Forward actuation mainly affected the cavitation area at the front edge of the suction side of the hydrofoil, where the shear motion and vortex motion were mutually restricted and transformed so that part of the vortex was transformed into shear flow. Reverse actuation eliminated most of the vortex and shear motion, and only the weak vortex motion existed in a small range at the leading edge of the hydrofoil; thus, reverse actuation suppressed hydrofoil cavitation and made the flow around it more stable.

5. CONCLUSION

In this study, the influence of plasma actuation on the cavitation characteristics of the NACA66(MOD) hydrofoil was studied via numerical analysis, and the main conclusions are as follows:

(1) The cavitation volume on the suction side of the hydrofoil was reduced by about 30% under the condition of forward actuation and by about 87% under the condition of reverse actuation, which showed that a reasonable plasma actuation method could effectively inhibit the development of cavitation on the surface of the hydrofoil.

(2) Under the condition of forward actuation, the time-averaged lift and drag ratio of the hydrofoil was reduced by about 5%, and the characteristic frequency of the lift coefficient was unchanged, but the vibration amplitude corresponding to the main frequency was increased by about 13%. Under the condition of reverse actuation, the time-averaged lift–drag ratio increased by about 21%, and the frequency spectrum characteristics of the lift coefficient changed, while the pulsation amplitude decreased significantly, indicating that forward actuation had little influence on the hydrodynamic characteristics of the hydrofoil, while reverse actuation effectively improved the hydrodynamic characteristics of the hydrofoil.

(3) Forward actuation suppressed the duration of the cloud cavitation and enhanced the shedding strength by weakening the pressure pulsation intensity in the front half and enhancing the pressure pulsation intensity in the back half of the hydrofoil suction surface. Reverse actuation improved the overall pressure on the suction side of the hydrofoil and improved the frequency spectrum characteristics of pressure pulsation, thus worsening the conditions for cavitation development and inhibiting cavitation development.

(4) Forward actuation could weaken the intensity of the re-entrant jet to a certain extent, but the cavitation and the re-entrant jet were still at the level of strong interaction; the inhibition effect on the development of cavitation was limited, while reverse actuation could obviously reduce the intensity of the re-entrant jet and its interaction with cavitation, thus achieving significant inhibition of cavitation in the hydrofoil flow field.

(5) The vortex region was in conformity with the outer contour region of the cavitation, and the shear region was in conformity with the outer contour region of the re-entrant jet region. Forward actuation mainly affected the cavitation region at the front edge of the suction side of the hydrofoil, making part of the vortex flow change into shear flow, while reverse actuation made the hydrofoil flow more stable while restraining hydrofoil cavitation.

ACKNOWLEDGEMENTS

This study was funded by the National Natural Science Foundation of China [Grant No. 52009050].

CONFLICT OF INTEREST

No potential conflicts of interest are reported by the authors.

AUTHORS CONTRIBUTION

Rong Guo: Conceptualization, Methodology, Writing—review and editing. **Luyi Wang**: Data curation, Writing—original draft. **Rennian Li**: Supervision. **Xuhao Zhang**: Investigation validation.

REFERENCES

Abdelraouf, H., Elmekawy, A. M. N., & Kassab, S. Z. (2020). Simulations of flow separation control numerically using different plasma actuator models. *Alexandria Engineering Journal*, *59*(5), 3881–3896. https://doi.org/10.1016/j.aej.2020.06.044

Coutier-Delgosha, O., Fortes-Patella, R., & Reboud, J. L. (2003). Evaluation of the turbulence model influence on the numerical simulations of unsteady cavitation. *Journal of Fluids Engineering, Transactions of the ASME*, *125*(1), 38–45. https://doi.org/10.1115/1.1524584

Deng, Y., Zhang, X., Im, N., & Liang, C. (2021). Compound learning tracking control of a switched fully-submerged hydrofoil craft. *Ocean Engineering*, *219*, 108260. https://doi.org/10.1016/j.oceaneng.2020.108260

Gu, Y., Zhang, J., Yu, S., Mou, C., Li, Z., He, C., Wu, D., Mou, J., & Ren, Y. (2022). Unsteady numerical simulation method of hydrofoil surface cavitation. *International Journal of Mechanical Sciences*, *228*, 107490. https://doi.org/10.1016/j.ijmecsci.2022.107490

Guo, G., Wang J., Zhang R., Chen, X., & Yang, J. (2022). Numerical study on plasma control of axial tip clear ance leakage flow in liquid ring pump. *Transactions of the Chinese Society for Agricultural Machinery*, *53*(9), 160–167. https://doi.org/10.6041/j.issn.1000-1298.2022.09.016

Kawanami, Y., Kato, H., Yamaguchi, H., Tanimura, M., & Tagaya, Y. (1997). Mechanism and control of cloud cavitation. *Journal of Fluids Engineering*, *119*(4), 788–794. https://doi.org/10.1115/1.2819499

Kumagai, I., Takahashi, Y., & Murai, Y. (2015). Power-saving device for air bubble generation using a hydrofoil to reduce ship drag: Theory, experiments, and application to ships. *Ocean Engineering*, *95*, 183–194. https://doi.org/10.1016/j.oceaneng.2014.11.019

Li, D., Miao, B., Li, Y., Gong, R., & Wang, H. (2021). Numerical study of the hydrofoil cavitation flow with thermodynamic effects. *Renewable Energy*, *169*, 894–904. https://doi.org/10.1016/j.renene.2021.01.073

Li, Y., Wu, Y., Liang, H., Zhu, Y., Zhang, H., & Guo, S. (2022). Exploration and outlook of plasma-actuated gas dynamics. *Advances in Mechanics*, *52*(1), 1–32. https://doi.org/10.6052/1000-0992-21-044

Liu, C., Yan, Q., & Wood, H. G. (2019). Numerical investigation of passive cavitation control using a slot on a three-dimensional hydrofoil. *International Journal of Numerical Methods for Heat & Fluid Flow*, *30*(7), 3585–3605. https://doi.org/10.1108/HFF-05-2019-0395

Look, A., Riedelbauch, S., Necker, J., & Jung, A. (2019). *Cavitation damage detection through acoustic emissions.* IOP Conference Series: Earth and Environmental Science, 405(1), 012004. https://doi.org/10.1088/1755-1315/405/1/012004

Pant, C. S., & Frankel, S. H. (2021). Interaction between surface blowing and re-entrant jet in active control of hydrofoil cavitation. *Ocean Engineering*, *242*, 110087. https://doi.org/10.1016/j.oceaneng.2021.110087

Podnar, A., Hočevar, M., Novak, L., & Dular, M. (2021). Analysis of bulb turbine hydrofoil cavitation. *Applied Sciences*, *11*(6), 2639. https://doi.org/10.3390/app11062639

Saurel, R., & Lemetayer, O. (2001). A multiphase model for compressible flows with interfaces, shocks, detonation waves and cavitation. *Journal of Fluid Mechanics*, *431*, 239–271. https://doi.org/10.1017/S0022112000003098

Schnerr, G. H., & Sauer, J. (2001). *Physical and numerical modeling of unsteady cavitation dynamics*. 4th International Conference on Multiphase Flow, New Orleans, USA.

Shyy, W., Jayaraman, B., & Andersson, A. (2002). Modeling of glow discharge-induced fluid dynamics. *Journal of Applied Physics*, *92*(11), 6434–6443. https://doi.org/10.1063/1.1515103

Thomai, M. P., & Chatterjee, D. (2015). Computational analysis of flow over a cascade of S-shaped hydrofoil of fully reversible pump-turbine used in extracting tidal energy. *Renewable Energy*, *77*, 240–249. https://doi.org/10.1016/j.renene.2014.12.019

Wang, W., Lu, S., Xu, R., Yi, Q., Wang, Y., & Wang, X. (2017). Numerical study of hydrofoil surface jet flow on cavitation suppression. *Journal of Drainage and Irrigation Machinery Engineering*, *35*(10), 829–834. https://doi.org/10. 3969 / j. issn. 1674 — 8530. 16. 1028

Wang, W., Tang, T., Lu, S., Zhang, Q., & Wang, X. (2019). Numerical simulation and analysis of active jet control of hydrofoil cavitation. *Chinese Journal of Theoretical and Applied Mechanics*, *51*(6), 1752–1760. https://doi.org/10.6052/0459-1879-19-222

Wang, W., Zhang, Q., Tang, T., An, Z., Tong, T., & Wang, X. (2020). Mechanism investigation of water injection on suppressing hydrofoil cloud cavitation flow. *Chinese Journal of Theoretical and Applied Mechanics*, *52*(1), 12–23. https://doi.org/10.6052/0459-1879-19-282

Wang, Y. C., & Brennen, C. E. (1999). Numerical computation of shock waves in a spherical cloud of cavitation bubbles. *Journal of Fluids Engineering*, *121*(4), 872–880. https://doi.org/10.1115/1.2823549

Wang, Y., Gao, C., Wu, B., & Hu, X. (2016). Simulation of flow around cylinder actuated by DBD plasma. *Plasma Science and Technology*, *18*(7), 768–774. https://doi.org/10.1088/1009-0630/18/7/12

Yang, N., Okajima, J., & Iga, Y. (2023). Change in cavitation regime on NACA0015 hydrofoil by heating the hydrofoil surface. *Journal of Fluids Engineering*, *145*(7), 071201. https://doi.org/10.1115/1.4057004

Yu, H., & Zheng, J. (2023). Investigation of flow separation control over airfoil using nanosecond pulsed plasma actuator. *International Journal of Heat and Mass Transfer*, *203*, 123786. https://doi.org/10.1016/j.ijheatmasstransfer.2022.123786

Zhang X., & Wang X. (2023). Research progress and outlook of flow field created by dielectric barrier discharge plasma actuators driven by a sinusoidal alternating current high-voltage power. *Chinese Journal of Theoretical and Applied Mechanics*, *55*(2), 285–298. https://doi.org/10.6052/0459-1879-22-377

Zhao, W., Liu, Z., Chen, S., Ding, Y., & Li, P. (2023). Research on regulation and optimization of hydrofoil cavitation flow field. *Journal of Xi'an Jiaotong University*, *5*, 1–12. https://doi.org/10.7652/xjtuxb202305008